A DSVM-Based MPC Strategy With Magnetizing Inductance Online Identification Method for Thrust Ripple Suppression in Linear Induction Machine

Yingcong Guo, Wei Xu, *Fellow, IEEE*, Jian Ge, *Member, IEEE*, Han Xiao,
Yirong Tang, *Student Member, IEEE*, and Yongdao Shangguan

***Abstract*—The conventional discrete space vector modulation-based model predictive control (DSVM-MPC) strategies in linear induction machines (LIMs) have two problems, one is that the current harmonics and thrust ripple are large as accuracy of the voltage vector (VV) is insufficient under the limited computational burden, and the other is that the parameter robustness is poor. To solve these problems, an improved DSVM-MPC strategy with magnetizing inductance online identification method for LIMs is proposed. First, an improved virtual VV discretization method and an optimal VV searching method are proposed, which can obtain more accurate VV with less computational burden compare to conventional DSVM-MPC strategies. Then, to improve the parameter robustness, a magnetizing inductance online identification method based on back electromotive force (EMF) is proposed, and a sliding mode observer (SMO) is designed to observe back EMF, which effectively avoids the current differential term. Furthermore, an adaptive compensation algorithm for cascaded low-pass filters is conceived to effectively suppress the inherent chattering of the SMO, and the amplitude and phase of the fundamental wave are appropriately compensated. Finally, the superiority of the proposed method is verified through comprehensive simulations and experiments on a 3kW LIM prototype.**

***Index Terms*—Discrete space vector modulation (DSVM), inductance identification, linear induction machine (LIM), model predictive control (MPC), thrust ripple.**

Received 28 September 2024; revised 13 January 2025 and 23 February 2025; accepted 25 March 2025. Date of publication 31 March 2025; date of current version 26 May 2025. This work was supported in part by the National Natural Science Foundation of China under Grant 52277050 and Grant 52407050, in part by the High-level Talent Program at Chinese Academy of Sciences under Grant 2Q2024000076, in part by the Shenzhen Fundamental Research Project (General Program) under Grant JCYJ20230807143701003, and in part by the Fundamental Research Funds for the Central Universities under Grant YCJJ20242205. Recommended for publication by Associate Editor B. K. Lee. *(Corresponding author: Wei Xu.)*

Yingcong Guo is with the School of Electrical Engineering, Southwest Jiaotong University, Chengdu 610031, China (e-mail: yingcongguo@my.swjtu.edu.cn).

Wei Xu is with the Key Laboratory of High Density Electromagnetic Power and Systems (Chinese Academy of Sciences), Institute of Electrical Engineering, Chinese Academy of Sciences, Beijing 100190, China (e-mail: weixu@mail.iee.ac.cn).

Jian Ge, Han Xiao, Yirong Tang, and Yongdao Shangguan are with the State Key Laboratory of Advanced Electromagnetic Technology, School of Electrical and Electronic Engineering, Huazhong University of Science and Technology, Wuhan 430074, China (e-mail: gejian1994@hust.edu.cn; xiaohan@hust.edu.cn; yirtang@hust.edu.cn; sgyd@hust.edu.cn).

Color versions of one or more figures in this article are available at https://doi.org/10.1109/TPEL.2025.3555708.

Digital Object Identifier 10.1109/TPEL.2025.3555708

NOMENCLATURE

$\boldsymbol{u}_{1\alpha\beta}$	$\boldsymbol{u}_{1\alpha\beta} = [u_{1\alpha}, u_{1\beta}]^{\mathrm{T}}$, $\alpha\beta$-axis primary voltages.
$\boldsymbol{i}_{1\alpha\beta}$	$\boldsymbol{i}_{1\alpha\beta} = [i_{1\alpha}, i_{1\beta}]^{\mathrm{T}}$, $\alpha\beta$-axis primary currents.
$\boldsymbol{i}_{2\alpha\beta}$	$\boldsymbol{i}_{2\alpha\beta} = [i_{2\alpha}, i_{2\beta}]^{\mathrm{T}}$, $\alpha\beta$-axis secondary currents.
$\boldsymbol{\psi}_{2\alpha\beta}$	$\boldsymbol{\psi}_{2\alpha\beta} = [\psi_{2\alpha}, \psi_{2\beta}]^{\mathrm{T}}$, $\alpha\beta$-axis secondary fluxes.
$\boldsymbol{e}_{\mathrm{m}\alpha\beta}$	$\boldsymbol{e}_{\mathrm{m}\alpha\beta} = [e_{\mathrm{m}\alpha}, e_{\mathrm{m}\beta}]^{\mathrm{T}}$, $\alpha\beta$-axis back EMFs.
$\boldsymbol{i}_{\mathrm{m}\alpha\beta}$	$\boldsymbol{i}_{\mathrm{m}\alpha\beta} = [i_{\mathrm{m}\alpha}, i_{\mathrm{m}\beta}]^{\mathrm{T}}$, $\alpha\beta$-axis magnetizing currents.
F_{e}	Electromagnetic thrust.
$L_{1\sigma}$, $L_{2\sigma}$	Primary and secondary leakage inductances.
L_{m}	Magnetizing inductance.
R_1, R_2	Primary and secondary resistances.
k, $k+1$	k and $k+1$ instants.

Superscript

$*$	Reference value.
p	Predicted value.
^	Estimated value.

Subscript

1, 2	Variables for primary and secondary of LIM.
α, β	Components of $\alpha\beta$-axis.
d, q	Components of dq-axis.
ref	Reference model value.
adp	Adaptive model value.

I. INTRODUCTION

The linear induction machines (LIMs) derived from rotary induction machines (RIMs) can generate thrust in a straight direction without any conversion device [1]. Compared with RIMs, LIMs have many advantages, such as a simple mechanical structure, high reliability, fast acceleration and deceleration, which are very suitable for urban rail transit, industrial servo system, [2], [3]. The commonly used LIMs control strategies include vector control, direct thrust control, dead-beat control, model predictive control (MPC), and so on [4], [5], [6]. Among these control strategies, the MPC strategies have the advantages of fast dynamic response, simple implementation and flexible multiobjective control, and have been widely studied [7].

In ac motor control, it can be classified as continuous-control-set model predictive control (CCS-MPC) and finite-control-set model predictive control (FCS-MPC) based on the degree of state control in the switching devices. The CCS-MPC directly calculates the optimal voltage vector (VV) based on the cost function, which is error-free. Unfortunately, the CCS-MPC is usually used as a sub-link to replace the PI controller in vector control to achieve better response speed and decoupling. Compared to the FCS-MPC strategy, the CCS-MPC strategy demonstrates significantly higher complexity when addressing problems involving multiobjective optimization and multiconstraints [8], [9], as solving them through linear programming algorithms imposes a substantial computational burden. In contrast, FCS-MPC is simple and easy to implement, but conventional FCS-MPC strategies usually apply only one VV per control cycle. There is a large prediction error between the actual optimal VV and the applied VV, which produces large current harmonics and thrust ripple.

To suppress current harmonics and thrust ripple, dual-vector, and triple-vector MPC strategies are proposed by combining MPC strategies with voltage vector modulation [10], [11], [12]. These multivector control strategies increase the freedom in VV selection and improve the control performance, but are computationally intensive during each control cycle [7]. A simple and efficient discrete space vector modulation-based MPC (DSVM-MPC) strategy is proposed, which constructs multiple virtual VVs to search for the optimal VV [13] [14]. With the number of virtual VVs increases, the control performance of the system is significantly improved. However, it also increases the computational burden of the algorithm, causing time delay and reducing the control performance. To avoid this drawback, the corresponding optimal VV searching methods are proposed in [15], [16], and [17]. In [15], an independent searching method for the phase and amplitude of the optimal VV is designed, which further improves control accuracy and search efficiency, and provides a strict mathematical proof of the design principle. In [16], a VV discretization method based on the rhomboid center and an optimal VV searching method is proposed to reduce complexity. In [17], a modified bisection method is presented that saves approximately 66.7% of the computational burden compared to the dichotomy algorithm per iteration. However, due to the limited computational capability of microprocessors, the control performance improvement is limited. Thereof, further improvements are greatly desirable.

On the other hand, the MPC strategy is very sensitive to the model parameters, and the mismatched parameters will increase the prediction error and decrease the control performance [18]. Till now, main methods to improve the parameter robustness of MPC strategy have mainly included model-free predictive control (MFPC) strategy and parameter identification method. The MFPC strategies are not related to any structural information, and they are only designed from the input/output data of the controlled system, which are suitable for most kinds of electrical machines [19], [20], [21]. However, the secondary flux of LIMs needs to be observed, which is still affected by the magnetizing inductance. Hence, the MFPC strategies only apply to the predictive current controller, but the secondary flux observer is still affected by the parameter mismatch. Compared with RIMs, the LIMs feature the cut-open primary iron core, resulting in the end effect that cause nonlinear changes in the magnetizing inductance and other parameters, especially during high-speed region [22], [23]. Among these parameters, the magnetizing inductance which changes dramatically due to end effects has the greatest impact on the control performance [24]. Thereby, the magnetizing inductance identification methods may be more appropriate, and the magnetizing inductance identification methods of LIMs are studied [25], [26], [27], [28]. Currently, there are two main magnetizing inductance identification methods for LIMs, i.e., offline and online ones. Generally, the offline identification method is difficult to cover the changes of magnetizing inductance affected by all factors, such as primary iron core saturation and air-gap change [25], [26]. In [27], according to the T-type equivalent circuit in [23], a magnetizing inductance online identification method based on MARS is proposed, which takes secondary flux as the observation object, but its reference model is still affected by magnetizing inductance. Subsequently, the reference model established by back electromotive force (EMF) can avoid this drawback [28], but there is current differential term in the reference model, which is susceptible to current noise. Further improvement has been made by directly observing the back EMF with an extended state observer, which has a more accurate reference model, but the harmonic content of the observed back EMF is still large [5]. Thus, it is necessary to further investigate on a more practical and accurate magnetizing inductance online identification method to improve the parameter robustness of DSVM-MPC strategy.

Based on the abovementioned, to suppress the current harmonics and thrust ripple, a DSVM-MPC strategy with magnetizing inductance online identification method for LIM is presented.

The rest of this article is organized as follows. In Section II, the conventional FCS-MPC strategy of LIM is established. In Section III, a DSVM-MPC strategy is proposed, which includes a discretization method with high control performance and a searching method with less computational burden. In Section IV, a magnetizing inductance online identification method is proposed to improve the parameter robustness of DSVM-MPC. In Section V, comprehensive simulations and experiments are carried out on a 3 kW prototype, and the correctness and superiority of the proposed method is verified. Finally, Section VI concludes this article.

II. REVIEW OF CONVENTIONAL FCS-MPC STRATEGY FOR LIM

According to the T-type equivalent circuit of LIM proposed by Duncan [23], the primary current and secondary flux in the $\alpha\beta$-axis can be described as

$$\begin{cases} \frac{d\boldsymbol{i}_{1\alpha\beta}}{dt} = \frac{u_{1\alpha\beta}}{\sigma L_1} - \left(R_1 + \frac{R_2 L_m^2}{L_2^2}\right)\frac{\boldsymbol{i}_{1\alpha\beta}}{\sigma L_1} \\ + \left(\frac{R_2 L_m}{L_2^2} - j\frac{L_m}{L_2}\omega_2\right)\frac{\boldsymbol{\psi}_{2\alpha\beta}}{\sigma L_1} \\ \frac{d\boldsymbol{\psi}_{2\alpha\beta}}{dt} = \frac{R_2 L_m}{L_2}\boldsymbol{i}_{1\alpha\beta} - \frac{R_2}{L_2}\boldsymbol{\psi}_{2\alpha\beta} + j\omega_2\boldsymbol{\psi}_{2\alpha\beta} \end{cases} \tag{1}$$

where $\sigma = 1 - L_m^2/L_1L_2$, $L_1 = L_m + L_{1\sigma}$, $L_2 = L_m + L_{2\sigma}$, $\omega_2 = v_2\pi/\tau$, L_1, L_2, ω_2, v_2 and τ are the primary inductance, secondary inductance, secondary angular, speed and pole pitch, respectively.

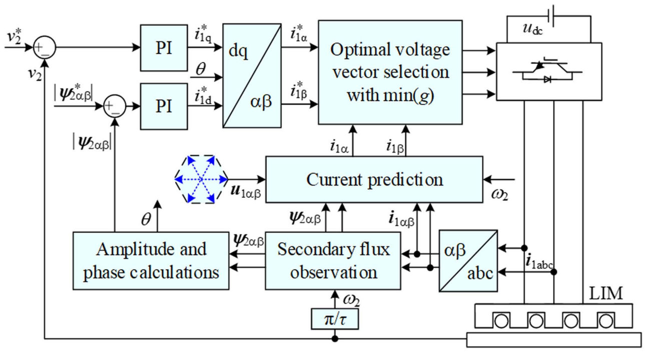

Fig. 1. Conventional FCS-MPC diagram of LIM.

The conventional FCS-MPC strategy diagram of LIM is shown in Fig. 1. Base on (1), the current prediction model and secondary flux prediction model of LIM can be expressed as

$$\begin{cases} \boldsymbol{i}_{1\alpha\beta}(k+1) = \frac{T_s}{\sigma L_1} \\ \left[\boldsymbol{u}_{1\alpha\beta}(k) + \left(\frac{\sigma L_1}{T_s} - R_1 - \frac{R_2 L_m^2}{L_2^2} \right) \boldsymbol{i}_{1\alpha\beta}(k) \right. \\ \left. + \left(\frac{R_2 L_m}{L_2^2} - j\frac{L_m}{L_2}\omega_2 \right) \boldsymbol{\psi}_{2\alpha\beta}(k) \right] \\ \boldsymbol{\psi}_{2\alpha\beta}(k+1) = T_s \left[\frac{R_2 L_m}{L_2} \boldsymbol{i}_{1\alpha\beta}(k) \right. \\ \left. - \left(\frac{R_2}{L_2} - \frac{1}{T_s} - j\omega_2 \right) \boldsymbol{\psi}_{2\alpha\beta}(k) \right] \end{cases} \tag{2}$$

where T_s is the control period.

Based on the prediction model, eight basic VVs are substituted into the pre-set cost function (3) to evaluate their control performance, and then the one with the smallest cost function will be selected as the optimal VV for the next control period

$$g = \left[i_{1\alpha}^* - i_{1\alpha}(k+2) \right]^2 + \left[i_{1\beta}^* - i_{1\beta}(k+2) \right]^2. \tag{3}$$

It can be seen from Fig. 1, the conventional FCS-MPC strategy has only eight basic VVs, and large voltage errors lead to high harmonic current content, resulting in large thrust ripple. Meanwhile, based on (2) and (3), the accuracy of secondary flux and current prediction heavily depends on the parameters of LIM. Once the parameters are mismatched, the control performance of the system will decrease to some extent.

III. IMPROVED DSVM-MPC STRATEGY WITH LESS COMPUTATIONAL BURDEN

To further reduce the current harmonics and thrust ripple within less computational burden, a virtual VV discretization method and an optimal VV searching method are presented in this section.

A. Virtual VV Discretization Method

The number of virtual VVs depends on the numbers of time intervals n and m in a control period T_s. The proposed space VV diagram is shown in Fig. 2, and the number of total virtual VVs n_{total} determined by

$$n_{\text{total}} = 2 \times 3^{n+m-1} \tag{4}$$

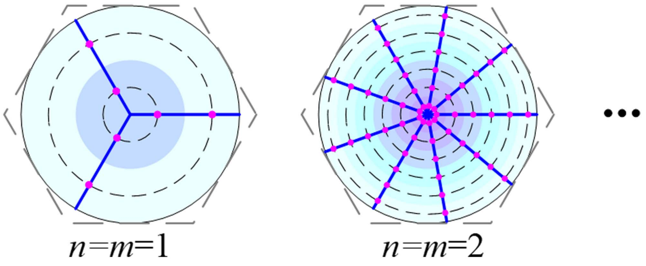

Fig. 2. Proposed spatial VV plane.

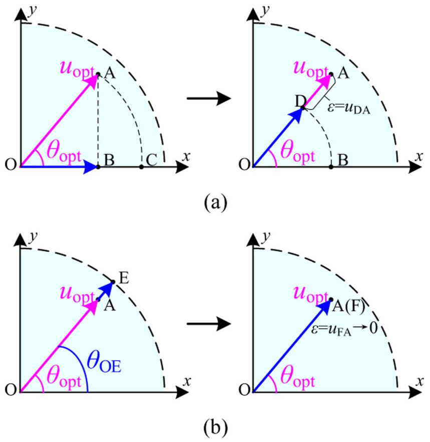

(a)

(b)

Fig. 3. Theoretical analysis of the searching method. (a) Case 1. (b) Case 2.

where n and m are positive integers, which can be adjusted separately to achieve appropriate control performance.

B. Theory of Optimal VV Searching Method

For the spatial VV plane described in Fig. 2, the searching of amplitude and phase in two independent stages. Fig. 3 describes two methods corresponding to different search orders, in which Fig. 3(a) searches the amplitude first, then the phase, and Fig. 3(b) searches the reverse order.

In Fig. 3, u_{opt} (OA) is the optimal VV in two search orders. In case 1, if the phase is assumed to be zero, |OB| is found as the applied amplitude with the minimized cost function. Subsequently, the amplitude is fixed to be |OB|, u_{OD} is found as the applied VV with the minimized cost function. Obviously, there is an error $\varepsilon = u_{\text{DA}}$ between u_{OD} and u_{opt}, and the error is 0 only if the assumed phase coincides with the phase of the optimal VV, which is almost impossible.

On the contrary, in case 2, the amplitude is set to $0.75u_m$ (u_m $=\sqrt{3}/3\ u_{\text{dc}}$, u_{dc} is the dc-link voltage), and θ_{OE} is found as the applied phase with the minimized cost function. Then, the phase is fixed to be θ_{OE}, u_{OF} is found as the applied VV with the minimized cost function. Theoretically, the error $\varepsilon = u_{\text{FA}}$ can be made to converge to 0 with a sufficiently large number of virtual VVs. Therefore, the above analysis proves that searching for phase firstly and then amplitude is the way to find the optimal VV.

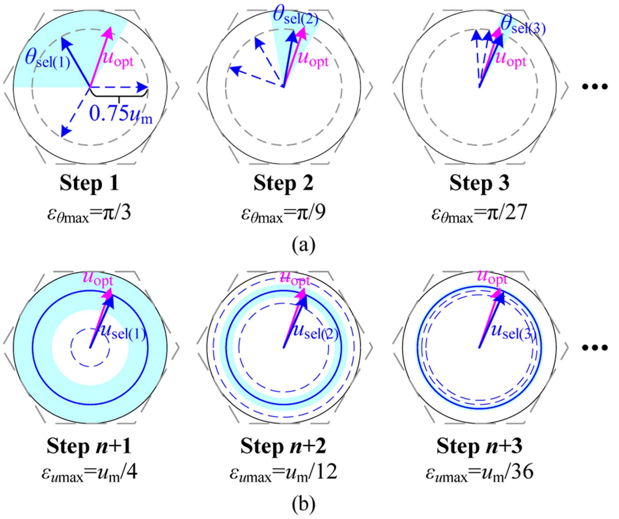

Fig. 4. Execution steps of the optimal VV searching method. (a) Steps to search the phase of the optimal VV. (b) Steps to search the amplitude of the optimal VV.

C. Execution Steps of Optimal VV Searching Method

In this subsection, the principle of the proposed optimal VV searching method will be introduced by explaining its execution steps. To clarify the proposed method, the actual optimal VV is set to u_{opt}, as shown in Fig. 4.

Steps to search the phase of the optimal VV: Step 1$\sim$step n, in which the vector length is set to $0.75u_m$. More details are summarized as follows.

Step 1: The three candidate voltage vectors (CVVs) with difference phase $2\pi/3$ are evaluated to find an optimal one with minimized cost function g, and its phase is recorded as $\theta_{\text{sel}(1)}$.

Step 2: The phase of three CVVs is set to $\theta_{\text{sel}(1)}$, $\theta_{\text{sel}(1)}+2\pi/9$ and $\theta_{\text{sel}(1)}\text{-}2\pi/9$, respectively, and evaluated to find the minimum cost function g, and its phase is recorded as $\theta_{\text{sel}(2)}$.

Step n: The phase of three CVVs is set to $\theta_{\text{sel}(n\text{-}1)}$, $\theta_{\text{sel}(n\text{-}1)}+2\pi/3^n$ and $\theta_{\text{sel}(n\text{-}1)}\text{-}2\pi/3^n$, respectively, and evaluated to find the minimum cost function g, and its phase is recorded as $\theta_{\text{sel}(n)}$.

By implementing Step n according to the above descriptions, the phase of VV $\theta_{\text{sel}(n)}$ with the smallest error from u_{opt} can be obtained, and the maximum relative error is $\varepsilon_{\theta\max}=\pi/3^n$.

Steps to search the amplitude of the optimal VV: Step n+1$\sim$Step n+m, in which the phase is set to $\theta_{\text{sel}(n)}$.

Step n+1: The amplitude of two CVVs is set to $0.25u_m$ and $0.75u_m$, and evaluated to find the minimum cost function g, and its amplitude is recorded as $u_{\text{sel}(1)}$.

Step n+2: The amplitude of three CVVs is set to $u_{\text{sel}(1)}$, $u_{\text{sel}(1)}+u_m/6$ and $u_{\text{sel}(1)}\text{-}u_m/6$, respectively, and evaluated to find the minimum cost function g, and its amplitude is recorded as $u_{\text{sel}(2)}$.

Step n+m: The amplitude of three CVVs is set to $u_{\text{sel}(m\text{-}1)}$, $u_{\text{sel}(m\text{-}1)}+u_m/(2\times3^{m\text{-}1})$ and $u_{\text{sel}(m\text{-}1)}\text{-}u_m/(2\times3^{m\text{-}1})$, respectively, and evaluated to find the minimum cost function g, and its amplitude is recorded as $u_{\text{sel}(m)}$.

TABLE I
COMPARISON WITH CONVENTIONAL METHODS

Methods	n_{total}	n_{CVV}	$n_{\text{total}}/n_{\text{CVV}}$
Conventional FCS-MPC strategy	8	8	1
Proposed method with *n* = *m* = 2	**54**	**8**	**6.75**
Method in [15] with $n=m=2$	48	13	3.69
Method in [16] with $n=3$	63	11	5.73
Method in [17] with $n=3$	96	12	8
Proposed method with *n* = *m* = 3	**486**	**12**	**40.5**

Similarly, the amplitude of VV $u_{\text{sel}(n)}$ with the smallest error from u_{opt} can be obtained, and the maximum relative error is $\varepsilon_{u\max}=u_m/(4\times3^{m\text{-}1})$.

Finally, the obtained optimal VV is transmitted to a PWM modulator to generate PWM signal. The whole spatial VV plane is discretized into $2\times3^{n+m\text{-}1}$ parts through n+m steps, and the number of total CVVs $n_{\text{CVV}}=2(n+m)$ needs to be evaluated.

D. Comparison With Conventional Methods

A comparison with conventional methods is made to indicate the advantages of the proposed optimal VV searching method, and the results are given in Table I. It can be clearly found that when n_{CVV} is similar, the proposed method divides more virtual VVs, which indicates the proposed method has higher accuracy.

IV. MAGNETIZING INDUCTANCE ONLINE IDENTIFICATION METHOD WITH STRONG PARAMETER ROBUSTNESS

It is proved that the mismatch of magnetizing inductance has a great influence on the control performance of MPC strategies. A magnetizing inductance online identification method with strong parameter robustness is proposed in this section.

A. Magnetizing Inductance Sensitivity Analysis

To visualize the impact of magnetizing inductance mismatched on prediction errors, assuming the magnetizing inductance in the controller is L_{mc}, the predicted primary currents and secondary fluxes can be given as

$$\begin{cases} \boldsymbol{i}^{\text{p}}_{1\alpha\beta}\left(k{+}1\right)=\frac{T_s}{\sigma_c L_{1c}} \\ \left[\begin{array}{l}\boldsymbol{u}_{1\alpha\beta}(k)+\left(\frac{\sigma_c L_{1c}}{T_s}-R_1-\frac{R_2 L^2_{\text{mc}}}{L^2_{2c}}\right)\boldsymbol{i}_{1\alpha\beta}(k) \\ +\left(\frac{R_2 L_{mc}}{L^2_{2c}}-j\frac{L_{mc}}{L_{2c}}\omega_2\right)\boldsymbol{\psi}_{2\alpha\beta}(k)\end{array}\right] \\ \boldsymbol{\psi}^{\text{p}}_{2\alpha\beta}\left(k{+}1\right)=T_s \\ \left[\frac{R_2 L_{mc}}{L_{2c}}\boldsymbol{i}_{1\alpha\beta}\left(k\right)-\left(\frac{R_2}{L_{2c}}-\frac{1}{T_s}+j\omega_2\right)\boldsymbol{\psi}_{2\alpha\beta}\left(k\right)\right] \end{cases} \tag{5}$$

where $L_{1c}=L_{mc}{+}L_{1\sigma}$, $L_{2c}=L_{mc}{+}L_{2\sigma}$ are the primary and secondary inductance in the controller, $\sigma_c=1-L^2_{mc}/L_{1c}L_{2c}$.

The prediction error of current $\Delta\boldsymbol{i}_{1\alpha\beta}$ and thrust can be expressed as

$$\begin{aligned}\Delta\boldsymbol{i}_{1\alpha\beta}&=\boldsymbol{i}^{\text{p}}_{1\alpha\beta}(k+1)-\boldsymbol{i}_{1\alpha\beta}(k+1)\\ &=\left(\frac{1}{\sigma_c L_{1c}}-\frac{1}{\sigma L_1}\right)T_{\text{s}}\boldsymbol{u}_{\alpha\beta}\left(k\right)\\ &\quad+\left[\left(\frac{R_1}{\sigma L_1}+\frac{R_2 L^2_m}{\sigma L_1 L^2_2}\right)-\left(\frac{R_1}{\sigma_c L_{1c}}+\frac{R_2 L^2_{\text{mc}}}{\sigma_c L_{1c} L^2_{2c}}\right)\right]\end{aligned}$$

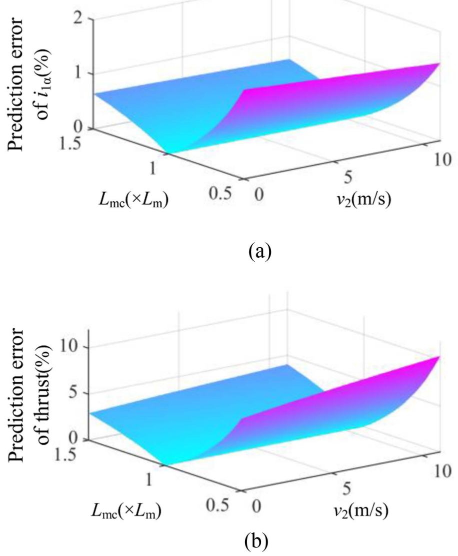

(a)

(b)

Fig. 5. Prediction error of thrust under different magnetizing inductance and speed. (a) Current. (b) Thrust.

$$T_s\boldsymbol{i}_{1\alpha\beta}\left(k\right) + \left[\begin{matrix}\left(\frac{R_2L_{mc}}{\sigma_cL_{1c}L_{2c}^2}-j\frac{L_{mc}}{\sigma_cL_{1c}L_{2c}}\omega_2\right)-\\ \left(\frac{R_2L_m}{\sigma L_1L_2^2}-j\frac{L_m}{\sigma L_1L_2}\omega_2\right)\end{matrix}\right]T_s\boldsymbol{\psi}_{2\alpha\beta}\left(k\right) \tag{6}$$

$$\Delta F_e = \frac{3\pi}{2\tau}\left[\boldsymbol{\psi}_{1\alpha\beta}^p\left(k{+}1\right)\otimes\boldsymbol{i}_{1\alpha\beta}^p\left(k{+}1\right) - \boldsymbol{\psi}_{1\alpha\beta}\left(k{+}1\right)\otimes\boldsymbol{i}_{1\alpha\beta}\left(k{+}1\right)\right] \tag{7}$$

where $\psi_{1\alpha\beta}$ are the $\alpha\beta$-axis primary fluxes, which can be derived from secondary fluxes, $\boldsymbol{\psi}_{1\alpha\beta} = \frac{L_m}{L_2}\boldsymbol{\psi}_{2\alpha\beta} + \sigma L_1\boldsymbol{i}_{1\alpha\beta}$.

For the convenience of analyzing prediction error, it is assumed that $\boldsymbol{u}_1(10{,}0)$ is the optimal VV acting on the inverter in the current period, $\psi_{2\alpha} = 0.3\cos\theta$ Wb, $\psi_{2\beta} = 0.3\sin\theta$ Wb, $i_{1\alpha} = 22\cos\theta$ A, $i_{1\beta} = 22\sin\theta$ A, $\theta = \pi/4$, and the sampling period T_s is 0.0002 s. The prediction errors for current and thrust are shown in Fig. 5, illustrating the effect of the magnetizing inductance mismatch. From (3), inaccurately predicted currents affect the cost function calculation and VV selection, which can generate additional current harmonics and thrust ripple.

B. Magnetizing Inductance Online Identification Method Based on SMO

From (1), the secondary flux model can be derived as

$$\frac{d\boldsymbol{\psi}_{2\alpha\beta}}{dt} = \frac{L_2}{L_m}\left(\boldsymbol{u}_{1\alpha\beta} - R_1\boldsymbol{i}_{1\alpha\beta} - \sigma L_1\frac{d\boldsymbol{i}_{1\alpha\beta}}{dt}\right). \tag{8}$$

With (8) as the reference model and the secondary flux in (1) as the adaptive model, combined with the appropriate adaptive law, the principle magnetizing inductance online identification method based on MRAS is drawn as Fig. 6.

However, it can be seen from (8) that the secondary flux is affected by the magnetizing inductance and is not a reference model in the true sense. Then, the pure integrator is also needed to compute the secondary flux. To eliminate the above defects, the back EMF is defined as the observed quantity [28], as given by

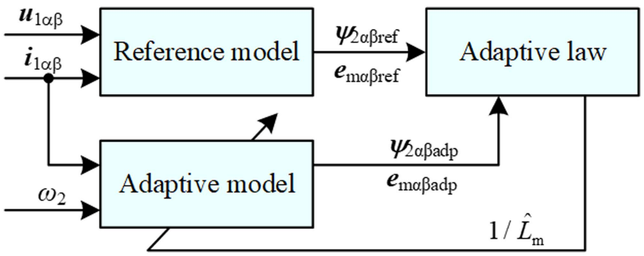

Fig. 6. Diagram of online identification method for magnetizing inductance.

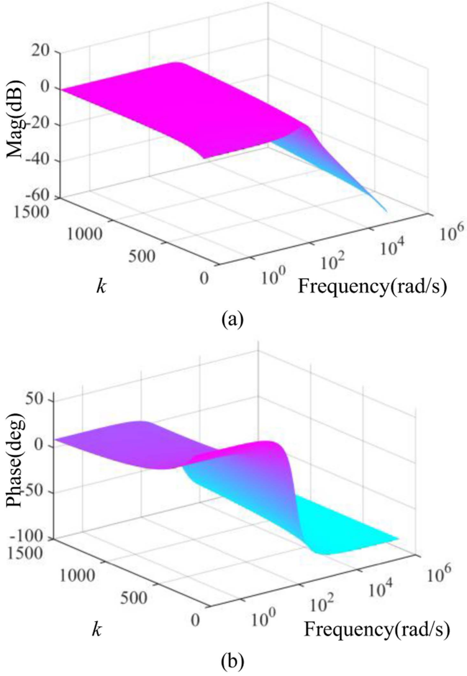

(a)

(b)

Fig. 7. Bode plots of the transfer function. (a) Magnitude. (b) Phase.

$$\boldsymbol{e}_{m\alpha\beta ada} = \frac{L_m}{L_2}\frac{d\boldsymbol{\psi}_{2\alpha\beta}}{dt} = \boldsymbol{u}_{1\alpha\beta} - R_1\boldsymbol{i}_{1\alpha\beta} - \sigma L_1\frac{d\boldsymbol{i}_{1\alpha\beta}}{dt} \tag{9}$$

where $\sigma L_1 {\approx} L_{1\sigma}{+}L_{2\sigma}L_{m0}/(L_{2\sigma}{+}L_{m0})$, L_{m0} is the magnetizing inductance with standstill LIM.

The adaptive model can be derived by

$$\begin{aligned}\boldsymbol{e}_{m\alpha\beta adp} &= \frac{\hat{L}_m^2}{\hat{L}_2}\frac{d\boldsymbol{i}_{m\alpha\beta}}{dt}\\ &= \frac{\hat{L}_m^2}{\hat{L}_2}\left(j\omega_2\boldsymbol{i}_{m\alpha\beta} - \frac{R_2}{\hat{L}_2}\boldsymbol{i}_{m\alpha\beta} + \frac{R_2}{\hat{L}_2}\boldsymbol{i}_{1\alpha\beta}\right)\end{aligned} \tag{10}$$

where $\boldsymbol{i}_{m\alpha\beta} = \boldsymbol{i}_{1\alpha\beta}{+}(L_2/L_m)\boldsymbol{i}_{2\alpha\beta}$.

The adaptive law is designed as

$$\frac{1}{\hat{L}_m} = \left(k_p + \frac{k_i}{s}\right)\left(\hat{\mathbf{e}}_{m\alpha\beta\mathrm{ref}} - \boldsymbol{e}_{m\alpha\beta ada}\right)^{\mathrm{T}}\hat{\mathbf{e}}_{m\alpha\beta\mathrm{ref}} \tag{11}$$

where k_p and k_i are positive numbers and s is a differential operator.

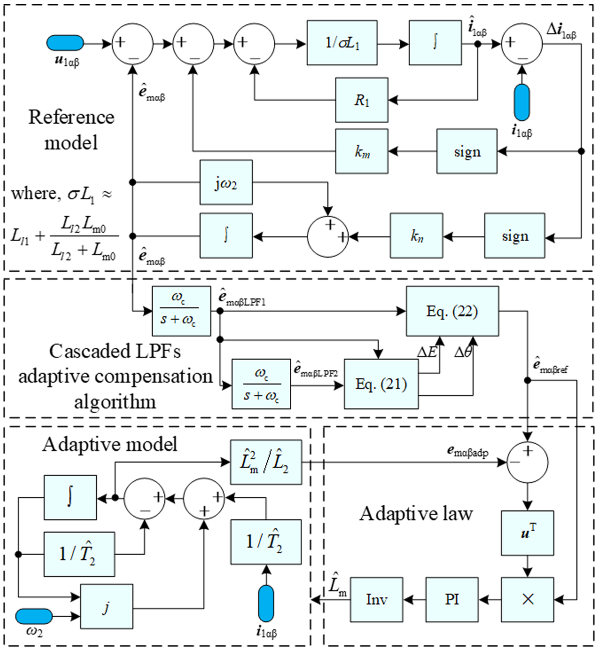

Fig. 8. Diagram of the proposed magnetizing inductance identification method.

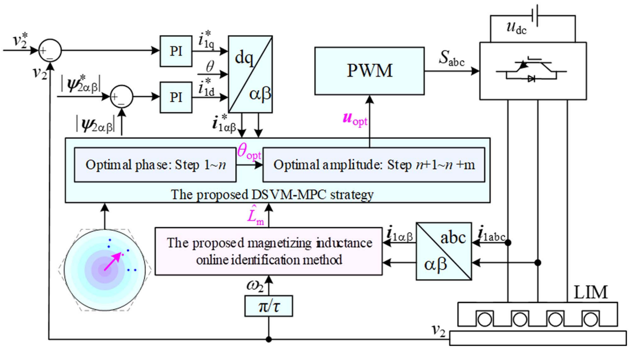

Fig. 9. Overall control block of the proposed method.

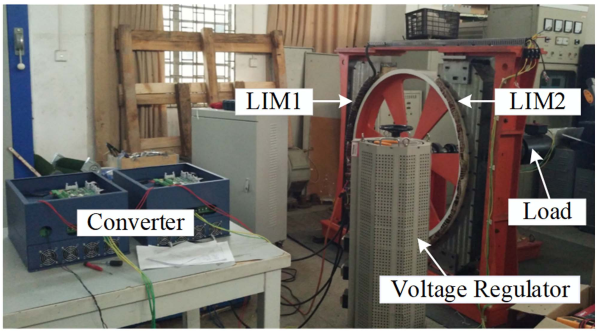

Fig. 10. LIM experimental platform.

However, for the reference model given by (9), there is also a differential term of current, which deteriorates the accuracy of magnetizing inductance identification. To overcome this problem, an SMO is designed to obtain the reference back EMF. The voltage model (9) can be rearranged as

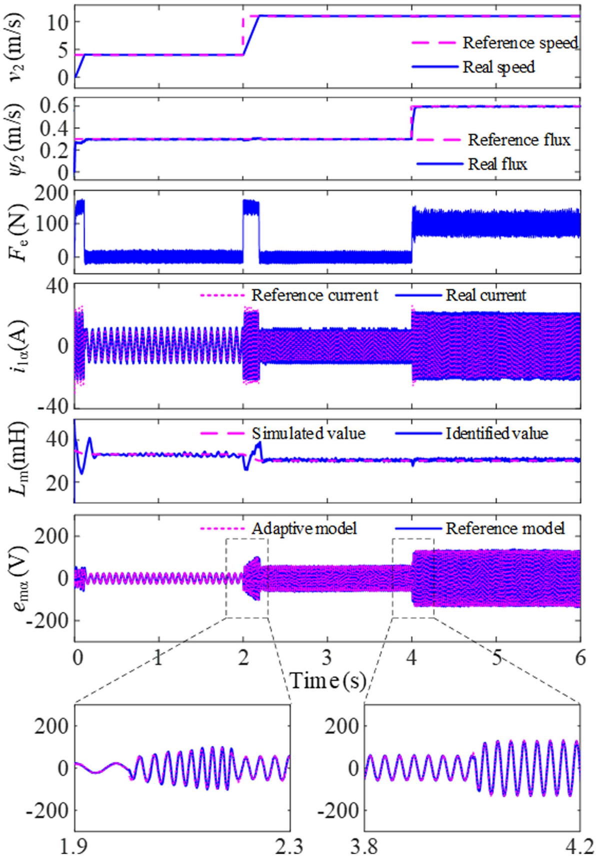

Fig. 11. Simulation results of the proposed identification method.

$$\frac{d\boldsymbol{i}_{1\alpha\beta}}{dt} = \frac{1}{\sigma L_1}\left(-R_1\boldsymbol{i}_{1\alpha\beta} + \boldsymbol{u}_{1\alpha\beta} - \boldsymbol{e}_{m\alpha\beta}\right). \tag{12}$$

Considering the back EMF is a sinusoidal signal, it can be described as

$$\frac{d\boldsymbol{e}_{m\alpha\beta}}{dt} = j\omega_2\boldsymbol{e}_{m\alpha\beta}. \tag{13}$$

According to (12) and (13), the reference model based on SMO is designed as

$$\begin{cases} \frac{d\hat{\boldsymbol{i}}_{1\alpha\beta}}{dt} = \frac{1}{\sigma L_1} \\ \left[-R_1\hat{\boldsymbol{i}}_{1\alpha\beta} + \boldsymbol{u}_{1\alpha\beta} - \hat{\mathbf{e}}_{m\alpha\beta} - k_m\text{sign}(\Delta\boldsymbol{i}_{1\alpha\beta})\right] \\ \frac{d\hat{\mathbf{e}}_{m\alpha\beta}}{dt} = j\omega_2\hat{\mathbf{e}}_{m\alpha\beta} + k_n\text{sign}(\Delta\boldsymbol{i}_{1\alpha\beta}) \end{cases} \tag{14}$$

where k_m and k_n are SMO paraments, $\Delta\boldsymbol{i}_{1\alpha\beta} = \hat{\boldsymbol{i}}_{1\alpha\beta} - \boldsymbol{i}_{1\alpha\beta}$, and sign() is a symbolic function. From (12)~(14), the estimation error can be derived by

$$\begin{cases} \frac{d\Delta\boldsymbol{i}_{1\alpha\beta}}{dt} = \frac{1}{\sigma L_1}\left[-R\Delta\boldsymbol{i}_{1\alpha\beta} - \Delta\boldsymbol{e}_{m\alpha\beta} - k_m\text{sign}(\Delta\boldsymbol{i}_{1\alpha\beta})\right] \\ \frac{d\Delta\boldsymbol{e}_{m\alpha\beta}}{dt} = j\omega_2\Delta\boldsymbol{e}_{m\alpha\beta} + k_n\text{sign}(\Delta\boldsymbol{i}_{1\alpha\beta}) \end{cases} \tag{15}$$

where $\Delta\boldsymbol{e}_{m\alpha\beta} = \hat{\mathbf{e}}_{m\alpha\beta} - \boldsymbol{e}_{m\alpha\beta}$.

To ensure that the current estimation error converges to 0, the gain k_m of SMO must meet condition $\Delta\boldsymbol{i}_{1\alpha\beta}\times(d\Delta\boldsymbol{i}_{1\alpha\beta}/\text{d}t)<0$,

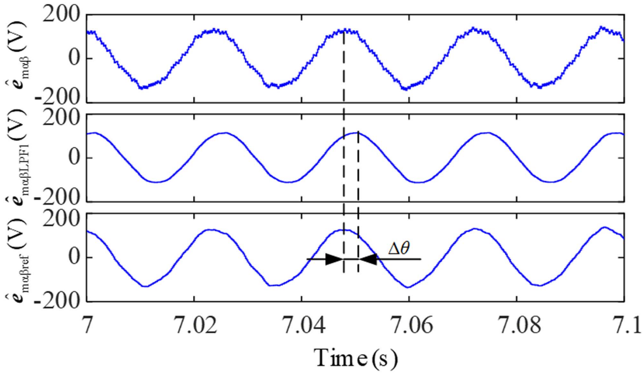

Fig. 12. Simulation results of the proposed adaptive compensation algorithm.

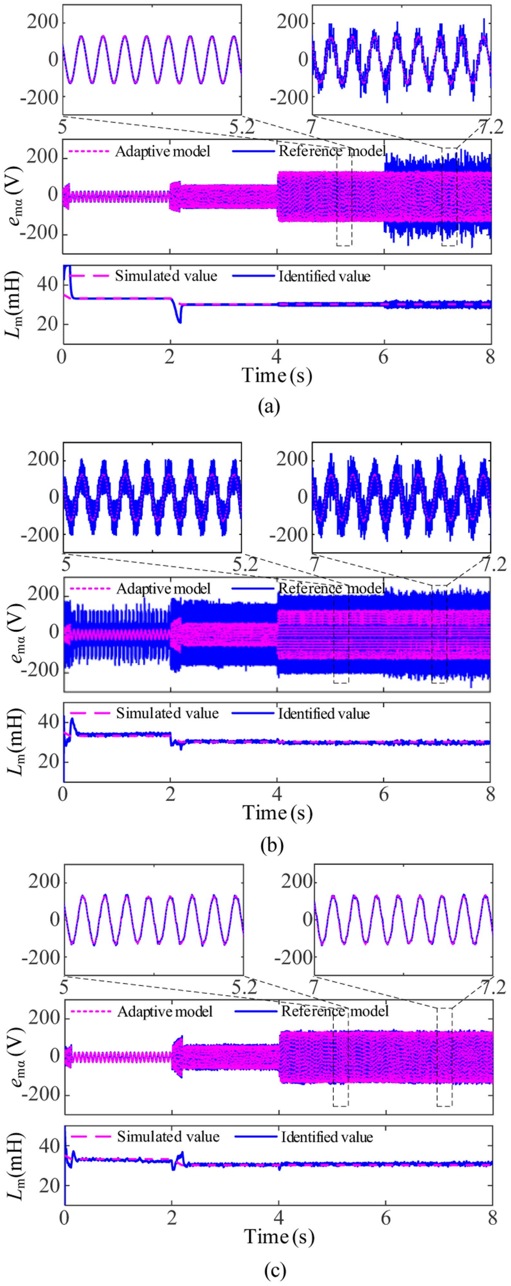

(a)

(b)

(c)

Fig. 13. Simulation results of different methods. (a) Method in [28]. (b) Method in [5]. (c) Proposed method.

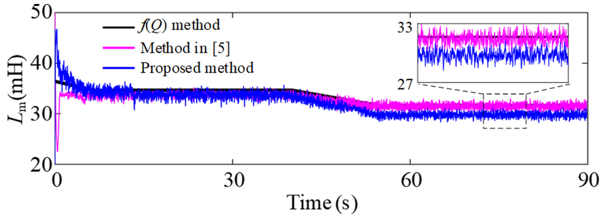

Fig. 14. Dynamic experimental results of magnetizing inductance identification.

which can be derived as

$$\begin{cases} k_m > -R\Delta \boldsymbol{i}_{1\alpha\beta} - \Delta \boldsymbol{e}_{m\alpha\beta}, & \Delta \boldsymbol{i}_{1\alpha\beta} > 0 \\ k_m > R\Delta \boldsymbol{i}_{1\alpha\beta} + \Delta \boldsymbol{e}_{m\alpha\beta}, & \Delta \boldsymbol{i}_{1\alpha\beta} < 0 \end{cases}. \tag{16}$$

Thus, the value range of k_m can be considered as k_m>0. If the current estimation error converges to 0, it can be deduced from (14) and (15) as

$$s\hat{\mathbf{e}}_{m\alpha\beta} = j\omega_2\hat{\mathbf{e}}_{m\alpha\beta} - \frac{k_n}{k_m}\left(\hat{\mathbf{e}}_{m\alpha\beta} - \boldsymbol{e}_{m\alpha\beta}\right). \tag{17}$$

Furthermore, by rearranging (17), the transfer function can be obtained as

$$G_1(s) = \frac{\hat{\mathbf{e}}_{m\alpha\beta}}{\boldsymbol{e}_{m\alpha\beta}} = \frac{k}{s + k - j\omega_2} \tag{18}$$

where $k = k_n/k_m$. To ensure that the designed SMO is stable, k>0 is required, that is, k_m and k_n are both positive. The Bode plots of the proposed observer is drawn as Fig. 7, where $\omega_2 = 233$ rad/s.

From Fig. 7(a), the high-frequency signal can be well reduced in the whole value range of k. Furthermore, when k is small, a certain low-frequency signal can be reduced. On the contrary, the transfer function bandwidth is larger, meaning the dynamic control performance is fast. Thus, a compromise must be made when choosing k.

C. Adaptive Compensation Algorithm for Cascaded LPFs

From (15), there are lots of sliding mode chattering signals generated by $k_m\text{sign}(\Delta\boldsymbol{i}_{1\alpha\beta})$ and $k_n\text{sign}(\Delta\boldsymbol{i}_{1\alpha\beta})$. Therefore, the LPFs are selected to filter out the sliding mode chattering, and an improved adaptive compensation method is designed to compensate the amplitude attenuation and phase delay of the fundamental wave caused by LPFs. There are two identical LPFs, and the transfer function can be described as

$$G_{\text{LPF}}(s) = \frac{\omega_c}{s + \omega_c} \tag{19}$$

where ω_c is the cutoff angular frequency of LPF. Through two cascaded LPFs, the estimated back EMF can be expressed as

$$\hat{\mathbf{e}}_{m\alpha\beta\text{LPF2}} = G_{\text{LPF}}\hat{\mathbf{e}}_{m\alpha\beta\text{LPF1}} = {G_{\text{LPF}}}^2\hat{\mathbf{e}}_{m\alpha\beta} \tag{20}$$

where $\hat{\mathbf{e}}_{m\alpha\beta\text{LPF1}} = [\hat{e}_{m\alpha\text{LPF1}}, \hat{e}_{m\beta\text{LPF1}}]^{\text{T}}$ and $\hat{\mathbf{e}}_{m\alpha\beta\text{LPF2}} = [\hat{e}_{m\alpha\text{LPF2}}, \hat{e}_{m\beta\text{LPF2}}]^T$ are estimated back EMF through a single LPF and two cascaded LPFs, respectively.

By using LPFs, $\hat{\mathbf{e}}_{m\alpha\beta\text{LPF1}}$ and $\hat{\mathbf{e}}_{m\alpha\beta\text{LPF2}}$ have no high-frequency sliding mode chattering. However, the LPF can cause amplitude attenuation and phase delay in the filtered wave.

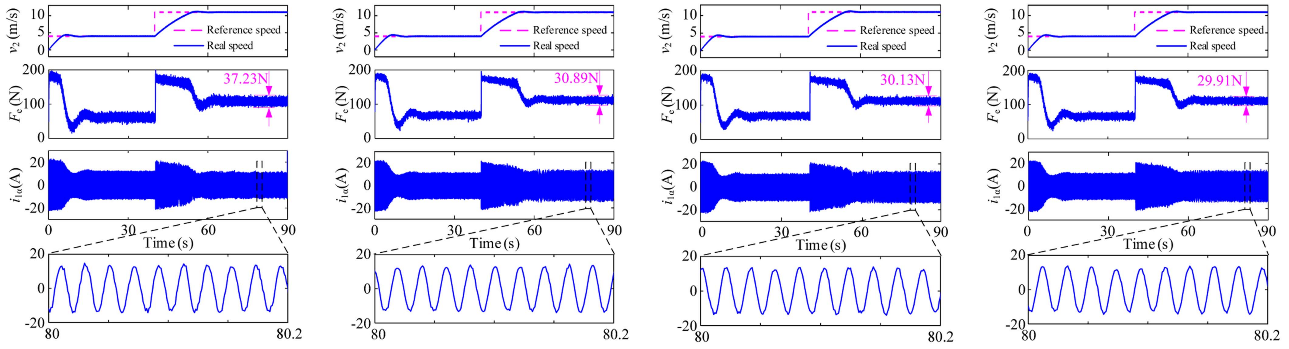

(a)

(b)

(c)

(d)

Fig. 15. Experimental results of control performance. (a) *f*(*Q*) method with 0.5×L_m. (b) *f*(*Q*) method with accurate L_m. (c) Method in [5]. (d) Proposed method.

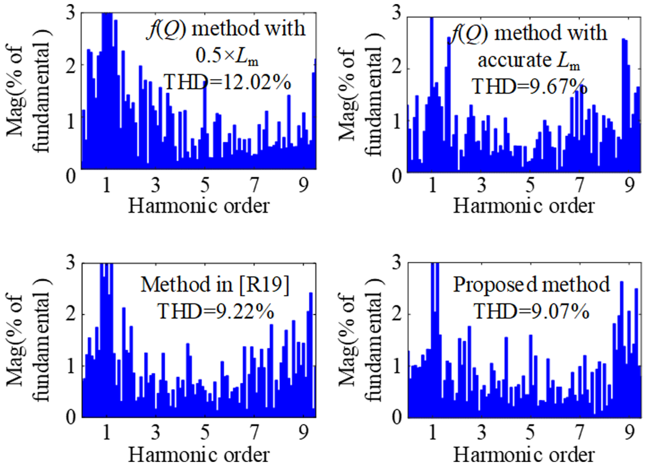

Fig. 16. FFT spectrum of current under different methods at rated speed.

Considering that the amplitude attenuation and phase delay of the same filter are the same, it is possible to design cascaded LPFs in reverse to derive the amplitude attenuation and phase delay, as given by

$$\begin{cases} \Delta E = \dfrac{E_{\text{LPF1}}}{E_{\text{LPF2}}} = \dfrac{\sqrt{\hat{e}^2_{m\alpha\text{LPF1}} + \hat{e}^2_{\text{m}\beta\text{LPF1}}}}{\sqrt{\hat{e}^2_{m\alpha\text{LPF2}} + \hat{e}^2_{\text{m}\beta\text{LPF2}}}} \\ \Delta\theta = \theta_{\text{LPF1}} - \theta_{\text{LPF2}} = \tan^{-1}\left(\dfrac{\hat{e}_{\text{m}\beta\text{LPF1}}}{\hat{e}_{m\alpha\text{LPF1}}}\right) \\ -\tan^{-1}\left(\dfrac{\hat{e}_{\text{m}\beta\text{LPF2}}}{\hat{e}_{m\alpha\text{LPF2}}}\right) \end{cases}. \tag{21}$$

Further, the filtered estimated back EMF $\hat{e}_{m\alpha\beta\text{LPF1}}$ is compensated by ΔE and $\Delta\theta$, as expressed as

$$\hat{e}_{m\alpha\beta\text{ref}} = \hat{e}_{m\alpha\beta\text{LPF1}} \Delta E \angle \Delta\theta. \tag{22}$$

Finally, a back EMF $\hat{e}_{m\alpha\beta\text{ref}}$without sliding mode chattering, amplitude attenuation, and phase delay can be obtained.

E. Overall System Construction

The control block of the proposed magnetizing inductance online identification method is shown in Fig. 8. Fig. 9 illustrates the overall control block of the proposed method, which contains the proposed DSVM-MPC strategy with the magnetizing inductance online identification method.

TABLE II
MAIN PARAMETERS OF THE LIM

Quantity	Symbol	Value
Rated speed	v_2*	11 m/s
dc-link voltage	u_{dc}	440 V
Pole pitch	τ	0.1485 m
Primary length	l_s	1.3087 m
Primary resistance	R_1	1.06 Ω
Primary leakage inductance	$L_{1\sigma}$	9 mH
Secondary resistance	R_2	2.4 Ω
Secondary leakage inductance	$L_{2\sigma}$	3.8 mH
Magnetizing inductance with standstill LIM	L_{m0}	35 mH

V. SIMULATION AND EXPERIMENTAL VERIFICATION

To verify the effectiveness and superiority of the proposed DSVM-MPC strategy and the magnetizing inductance online identification method, numerical simulation and experimental tests are performed in this section.

The experimental platform is shown in Fig. 10, and main parameters of LIM are given out in Table II. Limited by the space, the motor is designed as an arc structure, which has a large radius to simulate the actual linear conditions [29]. The microprocessor of the converter is DSP TMS320F28335, and the sampling frequency is 5 kHz.

A. Simulations of Magnetizing Inductance Identification

The magnetizing inductance of LIM can be modified by the coefficient *f*(*Q*) in [23]. The typical operation condition is conducted, in which the reference speed changes as 4 to 11 m/s at 2 s, and the load changes as 0 to 100 N at 4 s, and the reference secondary flux changes from 0.3 to 0.6 Wb at 4 s. Here, *k* is selected by trial-and-error method as 400, and the cutoff angular frequency of the LPFs is set to 1350 rad/s. Main simulation results by the proposed magnetizing inductance online identification method are given in Fig. 11, and the simulation results of the proposed adaptive compensation algorithm proposed are shown in Fig. 12.

From Fig. 11, the speed and secondary flux of the motor can achieve a good tracking to the reference value throughout the running process. The current reaches 22 A for a short time at start-up, due to the thrust and flux needed to be established, especially when high thrust is required. When the actual speed

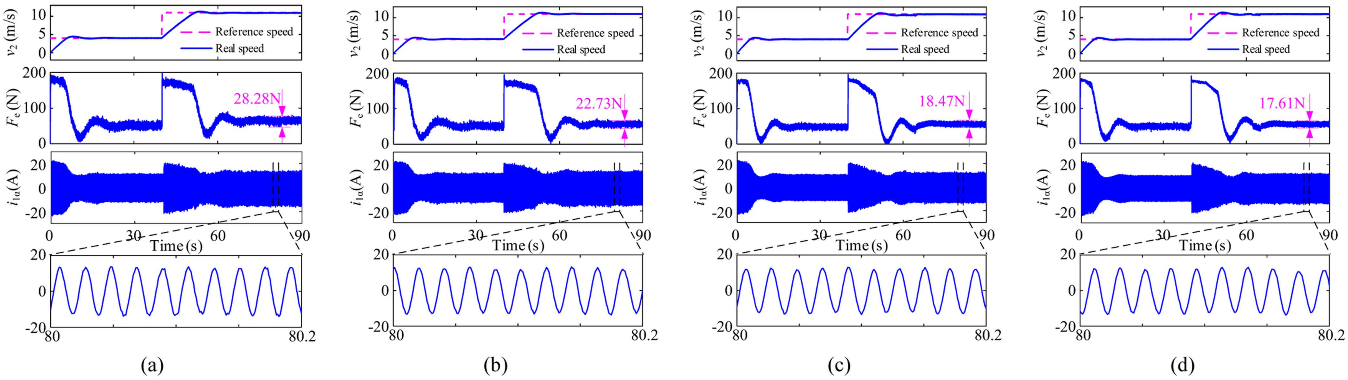

Fig. 17. Experimental comparisons of drive performance. (a) Conventional FCS-MPC strategy. (b) DSVM-MPC strategy in [16] with $n = 3$. (c) Proposed DSVM-MPC strategy with $n = m = 2$. (d) Proposed DSVM-MPC strategy with $n = m = 3$.

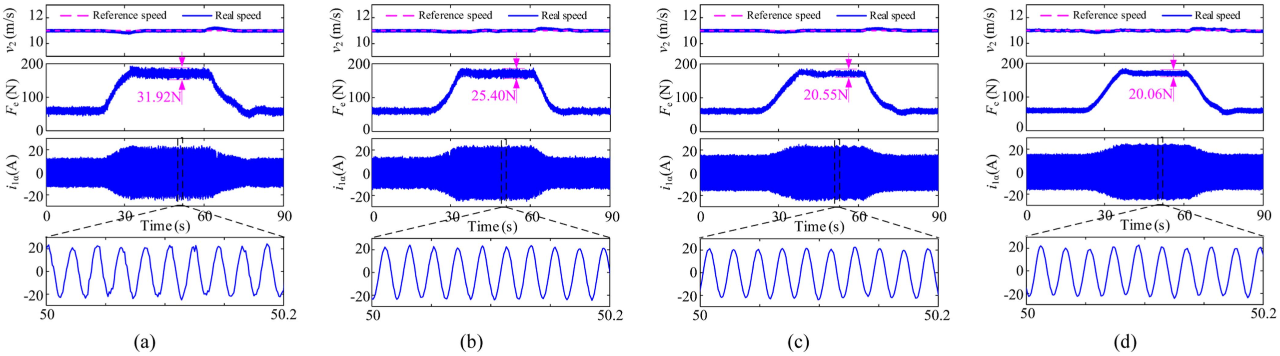

Fig. 18. Experimental comparisons of load change at rated speed 11 m/s. (a) Conventional FCS-MPC strategy. (b) DSVM-MPC strategy in [16] with $n = 3$. (c) Proposed DSVM-MPC strategy with $n = m = 2$. (d) Proposed DSVM-MPC strategy with $n = m = 3$.

reaches the reference speed, the current amplitude decreases and stabilizes. When the 100 N load is added at 4 s, the current and thrust increase simultaneously. In addition, the change trend of the adaptive back EMF is closely related to that of the reference back EMF. The identified magnetizing inductance are consistent with their simulated values very well. From Fig. 12, the proposed adaptive compensation algorithm effectively filters out a considerable amount of chattering generated by SMO, thereby compensating for the amplitude attenuation and phase delay of the fundamental wave caused by LPF.

Moreover, based on the above process, the current noise with a mean value of 0.5 A and a frequency of 2 kHz following a normal distribution are added at 6 s. Under the conventional FCS-MPC strategy, the proposed method is compared with the methods in [28] and [5], and the simulation results are shown in Fig. 13. In these figures, all these methods can match the magnetizing inductance in simulation before adding the current noise. However, the method in [28] is seriously impacted by current noise, while the method in [5] and the proposed method can effectively suppress the interference of current noise. This is attributed to the successful avoidance of the current differential term in the observer design. Compared with the method in [5], the reference model of the proposed method has less harmonic content of the back EMF, and the adaptive model is better matched with the estimated back EMF.

B. Experiments of Magnetizing Inductance Identification

In general, the magnetizing inductance of LIM is also affected by many factors, such as edge effect, primary core saturation, half-filled slot, and so on, while the $f(Q)$ coefficient factor cannot cover these factors simultaneously. To this end, experiments are needed to verify the correctness of the proposed identification method. In addition, the magnetizing inductance of LIM is not real as to be measurable. Therefore, the experimental results of the conventional FCS-MPC strategy combined with the $f(Q)$ method and different magnetizing inductance online identification methods, which can indirectly indicate the accuracy of the magnetizing inductance by the control performance.

Considering the difference between simulation and experimental tests, parameter k is reselected as 50 by trial-and-error method. Under the conventional FCS-MPC strategy, the dynamic experimental comparisons of magnetizing inductance identification are shown in Fig. 14, and the comparisons of experimental results are shown in Figs 15 and 16, corresponding to a predefined operating condition: the reference speed changes as 4 to 11 m/s at 40 s, and the load changes as 60 to 110 N at 40 s, and the reference secondary flux is set to 0.4 Wb.

From Fig. 14, referring to the $f(Q)$ method, the method in [5] and proposed method can effectively respond to the trend of the magnetizing inductance with working conditions. From Figs 15 and 16, the thrust ripple and current THD of the $f(Q)$ method with

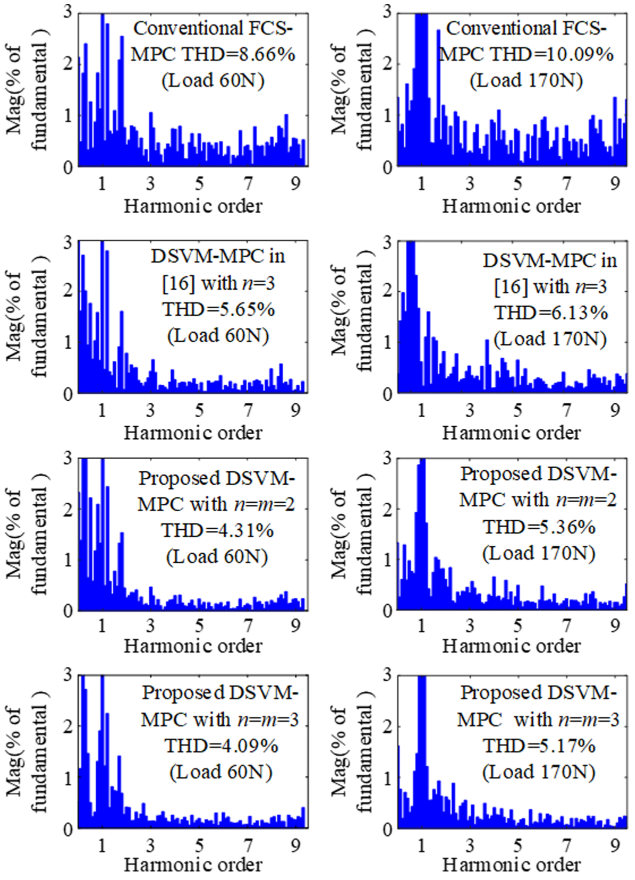

Fig. 19. FFT spectrum of current under different load at rated speed 11m/s.

$0.5\times L_m$ is significantly higher than that of the accurate L_m. This is explained by Fig. 5, where the parameter mismatch affects the predictive current calculation, increasing the error between the selected VV and the optimal VV. Moreover, compared to the $f(Q)$ method and the method in [5], the proposed method has fewer current THD and thrust ripple. Thereby, the control performance can indirectly show that the proposed method has more accurate magnetization inductance identification results.

C. Experimental Results of Control Performance

As aforementioned, the accuracy of the proposed magnetizing inductance online identification method has been fully proved by comprehensive simulations and experiments. In this section, different control methods will be employed to demonstrate the superiority of the proposed DSVM-MPC strategy.

Fig. 17 shows the comparisons of experimental results between the conventional FCS-MPC strategy, the DSVM-MPC strategy in [16] with $n = 3$, and the proposed DSVM-MPC strategy with $n = m = 2$ and $n = m = 3$, and the working conditions are set in advance: the reference speed changes as 4 to 11 m/s at 40 s, the load is set to 60 N, and the reference secondary flux is set to 0.4 Wb. In addition, Fig. 18 shows the dynamic change of load from 60 to 170 N and then to 60 N under the secondary flux of 0.7 Wb and the rated speed of 11 m/s. Fig. 19 shows the FFT spectrum of current under different load at rated speed.

As seen from Figs 17, 18, and 19, compared to the conventional FCS-MPC strategy, the DSVM-MPC strategy can significantly reduce the current THD and thrust ripple. Compared to method [16], the proposed DSVM-MPC strategy with $n = m = 2$ and $n = m = 3$ reduced the current THD by 23.7% and 27.6% and thrust ripple by 18.7% and 22.5% at light load. At heavy load, the proposed DSVM-MPC strategy with $n = m = 2$ and $n = m = 3$ reduced the current THD by 12.6% and 15.7%, and the thrust ripple by 19.1% and 21%. The above results show that the current THD and thrust ripple performance of the proposed DSVM-MPC strategy is better than that of method [16] under different working conditions. Meanwhile, it is further illustrated through Table I that the proposed method improves the accuracy of the applied VV under similar computational burden, which is the reason for its superiority.

Moreover, it is worth noting that although the current THD and thrust ripple can be further reduced with increasing n and m, this reduction trend tends to saturate. On other hand, due to the limitation of microprocessor computational capability, too large degree of discretization can cause system delays, which in turn lead to deterioration of the control performance. Thereby, $n = m = 3$ is the optimal solution in this article.

VI. CONCLUSION

This article presents a DSVM-MPC strategy with magnetizing inductance online identification method for LIM to further suppress the current harmonics and thrust ripple. Comprehensive simulations and experiments show that the proposed method has some advantages as follows.

1) To improve the parameter robustness of the MPC strategy, a magnetizing inductance online identification method based on back EMF observer is designed. The effect of the current differential term is avoided in the design of SMO, and the performance is better compared with methods in [5] and [28].
2) A novel adaptive compensation algorithm is proposed for cascaded LPFs to eliminate the inherent sliding mode chattering of SMO. Compared to a single LPF, the proposed method appropriately compensates the amplitude attenuation and phase delay of the filter.
3) Compared to similar methods in [15], [16], and [17], the proposed optimal VV searching method obtains more available VVs under the same computational burden, so that it has higher searching accuracy. As a result, the proposed control strategy has better performance with less current THD and thrust ripple.

REFERENCES

[1] I. Boldea, L. Tutelea, W. Xu, and M. Pucci, “Linear electric machines, drives and MAGLEVs: An overview,” *IEEE Trans. Ind. Electron.*, vol. 65, no. 9, pp. 7504–7515, Sep. 2018.

[2] R. Cao, M. Lu, N. Jiang, and M. Cheng, “Comparison between linear induction motor and linear flux-switching permanent-magnet motor for railway transportation,” *IEEE Trans. Ind. Electron.*, vol. 66, no. 12, pp. 9394–9405, Dec. 2019.

[3] A. K. Junejo, W. Xu, Y. Tang, K. Liao, H. Xiao, and Y. Li, “Enhanced cascade sliding mode direct thrust control for linear induction machine based on linear metro,” *IEEE Trans. Power Electron.*, vol. 39, no. 9, pp. 11517–11531, Sep. 2024.

[4] D. Hu, W. Xu, R. Dian, Y. Liu, and J. Zhu, "Loss minimization control of linear induction motor drive for linear metros," *IEEE Trans. Ind. Electron.*, vol. 65, no. 9, pp. 6870–6880, Sep. 2018.

[5] W. Xu et al., "Improved deadbeat predictive thrust control for linear induction machine with online parameter identification based on MRAS and linear extended state observer," *IEEE Trans. Ind. Appl.*, vol. 59, no. 3, pp. 3186–3199, May/Jun. 2023.

[6] W. Xu, Y. Tang, D. Dong, X. Xiao, E. E. M. Rashad, and A. K. Junejo, "Optimal reference primary flux based model predictive control of linear induction machine with MTPA and field-weakening operations for urban transit," *IEEE Trans. Ind. Appl.*, vol. 58, no. 4, pp. 4708–4721, Jul./Aug. 2022.

[7] J. Zou, W. Xu, J. Zhu, and Y. Liu, "Low-complexity finite control set model predictive control with current limit for linear induction machines," *IEEE Trans. Ind. Electron.*, vol. 65, no. 12, pp. 9243–9254, Dec. 2018.

[8] T. Geyer, "A comparison of control and modulation schemes for medium-voltage drives: Emerging predictive control concepts versus PWM-based schemes," *IEEE Trans. Ind. Appl.*, vol. 47, no. 3, pp. 1380–1389, May/Jun. 2011.

[9] Y. Zhang and W. Xie, "Low complexity model predictive control—Single vector-based approach," *IEEE Trans. Power Electron.*, vol. 29, no. 10, pp. 5532–5541, Oct. 2014.

[10] J. He, C. Wen, and X. Zhang, "Composite-bisection predictive control to stabilize and indirectly regulate downstream load inverters cascaded with LC input filters in the SPS," *J. Emerg. Sel. Topics Power Electron.*, vol. 9, no. 6, pp. 6854–6863, Dec. 2021.

[11] Y. Zhang, Y. Peng, and H. Yang, "Performance improvement of two-vectors-based model predictive control of PWM rectifier," *IEEE Trans. Power Electron.*, vol. 31, no. 8, pp. 6016–6030, Aug. 2016.

[12] Y. Tang, W. Xu, D. Dong, and X. Xiao, "MTPA based arbitrary double vectors model predictive thrust control without weighting factor for linear induction machine," in *Proc. Inter. Symp. Linear Drives Ind. Appl.*, 2021, pp. 1–6.

[13] Y. Zhang, H. Jiang, and H. Yang, "Model predictive control of PMSM drives based on general discrete space vector modulation," *IEEE Trans. Energy Convers.*, vol. 36, no. 2, pp. 1300–1307, Jun. 2021.

[14] J.-S. Lee, K.-B. Lee, and F. Blaabjerg, "Predictive control with discrete space-vector modulation of vienna rectifier for driving PMSG of wind turbine systems," *IEEE Trans. Power Electron.*, vol. 34, no. 12, pp. 12368–12383, Dec. 2019.

[15] L. Guo, H. Xiao, Y. Li, C. Yu, H. Xu, and K. Luo, "A DC-offset reduced grid-voltage sensorless model predictive control strategy for grid-tied inverters with a two-stage optimal voltage vector searching method," *IEEE Trans. Ind. Electron.*, vol. 70, no. 4, pp. 3920–3932, Apr. 2023.

[16] W. Xu et al., "Discrete space vector modulation-based MPCC with inductance identification for thrust ripple suppression in linear induction machine," *IEEE Trans. Power Electron.*, vol. 39, no. 10, pp. 12883–12893, Oct. 2024.

[17] J. He, C. Wen, and X. Zhang, "Composite-bisection predictive control to stabilize and indirectly regulate downstream load inverters cascaded with LC input filters in the SPS," *J. Emerg. Sel. Topics Power Electron.*, vol. 9, no. 6, pp. 6854–6863, Dec. 2021.

[18] T. T. Nguyen, H. N. Tran, T. H. Nguyen, and J. W. Jeon, "Recurrent neural network-based robust adaptive model predictive speed control for PMSM with parameter mismatch," *IEEE Trans. Ind. Electron.*, vol. 70, no. 6, pp. 6219–6228, Jun. 2023.

[19] C. Ma, H. Li, X. Yao, Z. Zhang, and F. De Belie, "An improved model-free predictive current control with advanced current gradient updating mechanism," *IEEE Trans. Ind. Electron.*, vol. 68, no. 12, pp. 11968–11979, Dec. 2021.

[20] Y. Zhang, T. Jiang, and J. Jiao, "Model-free predictive current control of a DFIG using an ultra-local model for grid synchronization and power regulation," *IEEE Trans. Energy Convers.*, vol. 35, no. 4, pp. 2269–2280, Dec. 2020.

[21] M. S. Mousavi, S. A. Davari, V. Nekoukar, C. Garcia, and J. Rodriguez, "Integral sliding mode observer-based ultralocal model for finite-set model predictive current control of induction motor," *J. Emerg. Sel. Topics Power Electron.*, vol. 10, no. 3, pp. 2912–2922, Jun. 2022.

[22] W. Xu, G. Sun, L. Wen, W. Wu, and P. Chu, "Equivalent circuit derivation and performance analysis of a single-sided linear induction motor based on the winding function theory," *IEEE Trans. Veh. Technol.*, vol. 61, no. 4, pp. 1515–1525, May 2012.

[23] J. Duncan, "Linear induction motor-equivalent-circuit model," *IEE Proc. B Elect. Power Appl.*, vol. 130, no. 1, pp. 51–57, Jan. 1983.

[24] D. Dong, W. Xu, X. Xiao, and Y. Liu, "Online magnetizing inductance identification strategy of linear induction motor based on second-order sliding-mode observer and MRAS," in *Proc. Int. Symp. Linear Drives Ind. Appl.*, 2021, pp. 1–6.

[25] F. Alonge, M. Cirrincione, F. D'Ippolito, M. Pucci, and A. Sferlazza, "Parameter identification of linear induction motor model in extended range of operation by means of input-output data," *IEEE Trans. Ind. Appl.*, vol. 50, no. 2, pp. 959–972, Mar./Apr. 2014.

[26] A. Accetta, M. Cirrincione, M. Pucci, and A. Sferlazza, "State-space vector model of linear induction machine including end-effects and iron losses-part II: Model identification and results," *IEEE Trans. Ind. Appl.*, vol. 56, no. 1, pp. 235–244, Jan./Feb. 2020.

[27] L. Liu, Y. Guo, and J. Wang, "Online identification of mutual inductance of induction motor without magnetizing curve," in *Proc. IEEE Annu. Amer. Control Conf.*, 2018, pp. 3293–3297.

[28] D. Dong, W. Xu, X. Xiao, Y. Tang, and K. Yang, "Online identification strategy of secondary time constant and magnetizing inductance for linear induction motors," *IEEE Trans. Power Electron.*, vol. 37, no. 10, pp. 12450–12462, Oct. 2022.

[29] J. Ge, W. Xu, Y. Liu, F. Xiong, and D. Li, "Investigation on winding theory for short primary linear machines," *IEEE Trans. Veh. Technol.*,. vol. 70, no. 8, pp. 7400–7412, Aug. 2021.

Yingcong Guo was born in Hunan, China. He received the B.S. and M.S. degrees in electrical engineering and automation from Xiangtan University, Xiangtan, China, in 2015 and 2018. He is currently working toward the Ph.D. degree in electrical engineering with the Southwest Jiaotong University, Chengdu, China.

From 2018 to 2021, he was a R&D Engineer with CRRC Zhuzhou Electric Co., Ltd., Zhuzhou, China. His research interests include design and control of linear motors and wind turbines.

Wei Xu (Fellow, IEEE) received the double B.E. and M.E. degrees from Tianjin University, Tianjin, China, in 2002 and 2005, respectively, and the Ph.D. degree from the Institute of Electrical Engineering, Chinese Academy of Sciences (IEECAS), Beijing, China, in 2008, all in electrical engineering.

From 2008 to 2012, he was a Post-Doctoral Fellow with the University of Technology Sydney, Ultimo, NSW, Australia, the Vice-Chancellor Research Fellow with the Royal Melbourne Institute of Technology, Melbourne, VIC, Australia, and a Japan Science Promotion Society Invitation Fellow with Meiji University, Tokyo, Japan, respectively. From 2013 to 2023, he was a Professor with the Huazhong University of Science and Technology, Wuhan, China. Since 2024, he has been a Professor with IEECAS. His research topics mainly focus on the design and control of linear machines and drives.

Dr. Xu is a Fellow of the Institute of Engineering and Technology. He was the General Chair of 2021 International Symposium on Linear Drives for Industry Applications and 2023 IEEE International Conference on Predictive Control of Electrical Drives and Power Electronics. He is an Associate Editor of more than ten peer-reviewed IEEE JOURNALS, including IEEE TRANSACTIONS ON INDUSTRIAL ELECTRONICS and IEEE TRANSACTIONS ON POWER ELECTRONICS.

Jian Ge (Member, IEEE) was born in Heilongjiang, China, in 1994. He received the B.E., M.E. and Ph.D degrees in electrical engineering from Huazhong University of Science and Technology, Wuhan, China, in 2016, 2019 and 2022, respectively.

He is currently a Postdoctoral Researcher in electrical engineering with Huazhong University of Science and Technology, Wuhan, China. His research interests include induction machines, linear machines, and brushless doubly-fed machines.

Han Xiao was born in Henan, China. He received the B.S. degree and M.S. degrees in electrical engineering and automation from Zhengzhou University of Light Industry, Zhengzhou, China, in 2019 and 2022. He is currently working toward the Ph.D. degree in electrical engineering with the Huazhong University of Science and Technology, Wuhan, China.

His research interests include model predictive control for linear induction machines and power converters.

Yirong Tang (Student Member, IEEE) received the B.E. degree in electrical engineering, in 2020, from Huazhong University of Science and Technology, Wuhan, China, where he is currently working toward the Ph.D. degree in electrical engineering with the State Key Laboratory of Advanced Electromagnetic Engineering and Technology.

His research interests include advanced control methods for linear induction machines, permanent magnet synchronous machines, and drives.

Yongdao Shangguan received the B.E. degree in marine electronic and electrical engineering from Dalian Maritime University, Dalian, China, in 2021. He is currently working toward the Ph.D. degree in electrical engineering with the School of Electrical Engineering, Huazhong University of Science and Technology, Wuhan, China.

His research interests include design and control of linear machines.